Experimental evaluation and basis function optimization of the spatially variant image-space PSF on the Ingenuity PET/MR scanner

Fotis A. Kotasidis[a)]
Division of Nuclear Medicine and Molecular Imaging, Geneva University Hospital, CH-1211 Geneva, Switzerland and Wolfson Molecular Imaging Centre, MAHSC, University of Manchester, Manchester M20 3LJ , United Kingdom

Habib Zaidi
Division of Nuclear Medicine and Molecular Imaging, Geneva University Hospital, CH-1211 Geneva, Switzerland; Geneva Neuroscience Centre, Geneva University, CH-1205 Geneva, Switzerland; and Department of Nuclear Medicine and Molecular Imaging, University of Groningen, University Medical Center Groningen, Groningen, 9700 RB, The Netherlands

(Received 10 October 2013; revised 4 April 2014; accepted for publication 22 April 2014; published 20 May 2014)

Purpose: The Ingenuity time-of-flight (TF) PET/MR is a recently developed hybrid scanner combining the molecular imaging capabilities of PET with the excellent soft tissue contrast of MRI. It is becoming common practice to characterize the system's point spread function (PSF) and understand its variation under spatial transformations to guide clinical studies and potentially use it within resolution recovery image reconstruction algorithms. Furthermore, due to the system's utilization of overlapping and spherical symmetric Kaiser-Bessel basis functions during image reconstruction, its image space PSF and reconstructed spatial resolution could be affected by the selection of the basis function parameters. Hence, a detailed investigation into the multidimensional basis function parameter space is needed to evaluate the impact of these parameters on spatial resolution.
Methods: Using an array of 12 × 7 printed point sources, along with a custom made phantom, and with the MR magnet on, the system's spatially variant image-based PSF was characterized in detail. Moreover, basis function parameters were systematically varied during reconstruction (list-mode TF OSEM) to evaluate their impact on the reconstructed resolution and the image space PSF. Following the spatial resolution optimization, phantom, and clinical studies were subsequently reconstructed using representative basis function parameters.
Results: Based on the analysis and under standard basis function parameters, the axial and tangential components of the PSF were found to be almost invariant under spatial transformations (∼4 mm) while the radial component varied modestly from 4 to 6.7 mm. Using a systematic investigation into the basis function parameter space, the spatial resolution was found to degrade for basis functions with a large radius and small shape parameter. However, it was found that optimizing the spatial resolution in the reconstructed PET images, while having a good basis function superposition and keeping the image representation error to a minimum, is feasible, with the parameter combination range depending upon the scanner's intrinsic resolution characteristics.
Conclusions: Using the printed point source array as a MR compatible methodology for experimentally measuring the scanner's PSF, the system's spatially variant resolution properties were successfully evaluated in image space. Overall the PET subsystem exhibits excellent resolution characteristics mainly due to the fact that the raw data are not under-sampled/rebinned, enabling the spatial resolution to be dictated by the scanner's intrinsic resolution and the image reconstruction parameters. Due to the impact of these parameters on the resolution properties of the reconstructed images, the image space PSF varies both under spatial transformations and due to basis function parameter selection. Nonetheless, for a range of basis function parameters, the image space PSF remains unaffected, with the range depending on the scanner's intrinsic resolution properties. [http://dx.doi.org/10.1118/1.4875689]

Key words: PET, image reconstruction, resolution recovery, basis functions, blobs

1. INTRODUCTION

The renewed interest in PET/MR imaging during the last few years, due to advancements in detector technology, has lead the main manufacturers to develop commercial whole body PET/MR systems.[1–3] These systems combine the excellent spatial resolution and soft tissue contrast of the MR, with the high sensitivity of the PET, to exploit their individual, as well as synergistic strengths in a number of clinical applications.[4,5] The combination of these two systems provide images of almost perfect spatial registration.[6,7] However, a number of technical challenges, both in the hardware and software domain, resulted in postponing their commercial introduction in clinical practice. In integrated PET/MR systems, like the

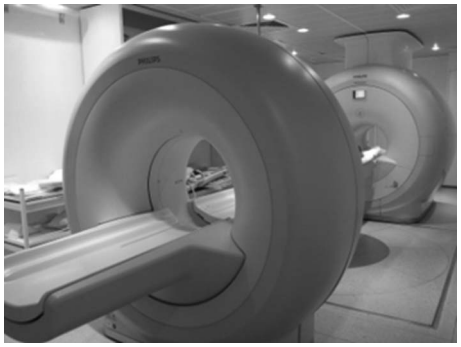

FIG. 1. The Philips Ingenuity TF PET/MR scanner is based on the Gemini TF PET and the Achieva 3T X-series MRI system and uses a rotating patient handling system to allow sequential scanning between the two modalities.

Siemens mMR, the two scanner components acquire simultaneous data within a common field-of-view (FOV).[3] On the other hand, one can maintain the technology currently used in PET and MR systems with minimal changes, by combining them in a tandem arrangement, allowing sequential acquisition between the two components.[2,8] The Philips Ingenuity TF PET/MR system falls in the latter category and uses a rotating patient handling system to enable sequential imaging between the two systems.[1] The scanner is comprised of the Gemini time-of-flight (TF) PET (Refs. 9 and 10) and the Achieva 3T X-series MRI systems (Fig. 1). Although the distance between the individual components (∼3 m) as well as the additional PMT and detector shielding, provide sufficient protection against interference effects,[11] detailed characterization of the scanner's point spread function (PSF) and resolution characteristics in the presence of the MR field is important. Such characterization could provide valuable information to guide clinical studies where spatial resolution is of importance and enable improved resolution recovery by taking into account the scanner's spatially variant PSF within resolution modeling image reconstruction algorithms.

Numerous aspects for estimating a scanner's PSF and applying it within statistical image reconstruction have been investigated.[12] Estimating the spatially variant PSF experimentally constitutes the most accurate approach and usually requires multiple acquisitions of a positron emitting source at discrete positions throughout the FOV.[13–17] However, conventional techniques based on robotic equipment are not feasible in PET/MR systems due to the need to operate within the magnetic field, provided the PSF measurements are performed with the magnet on. Therefore, other methods such as those based on positron beams or printed point sources can be used as fast and efficient alternatives.[14,18] Whether modeling the resolution characteristics in projection or in image space, rotation, and translation symmetries can be taken into account to reduce the locations where the PSF needs to be sampled. Modeling the PSF in image space is less challenging from an experimental setup point of view, while multiple points can be used to simultaneously sample the PSF at different locations in the FOV. At the same time, due to the parameterization of the measured response and the subsequent interpolation of the parameters in the remaining positions, image-based methods yield similar results to projection-based modeling when used within resolution recovery based image reconstruction algorithms.[12,14] Furthermore, as modeling and application of the spatially invariant/variant kernels occurs in image space, these methods are suitable for systems with list-mode image reconstruction due to the lack of a projection space.[19] In the Ingenuity TF PET/MR system, image reconstruction is performed on list-mode data, therefore image space modeling constitutes the method of choice for measuring the scanner's PSF.

Image reconstruction algorithms in PET aim to approximate the underlying activity distribution by representing it as a linear sum of shifted and scaled copies of a basis function (BF). Traditionally, estimating the image space blurring matrix requires the reconstruction of high statistics point source data using cubic basis functions (voxels) and modeling the reconstructed kernels using, in most cases, Gaussian functions to estimate a number of parameters. If statistical reconstruction is used, the algorithm should be iterated sufficiently for the data to approach convergence, in order to avoid further blurring of the kernels. Furthermore, post-reconstruction operations, such as filtering or any other operation that can impact spatial resolution, should also be avoided to prevent masking the true PSF. An image space PSF map can then be derived, which can be approximated as being independent of the reconstruction parameters. However, an alternative to the traditional cubic basis functions in image reconstruction is to use overlapping and smoothly decreasing spherically symmetric basis functions (blobs).[20] A common family of spherically symmetric basis functions used in image reconstruction is the Kaiser-Bessel window functions. The properties of these basis functions as opposed to cubic basis functions, can be adjusted by altering a set of parameters.[21] When such overlapping basis functions are used within image reconstruction, parameter selection has a profound effect on the properties of the reconstructed images.[22] Parameter optimization based on minimizing the error by which a constant function can be reconstructed has been used in the past.[23] However, since such basis functions were originally introduced to improve signal to noise ratio, previous studies have mainly concentrated on the variance characteristics of the reconstructed images, while basis function parameters could also have an effect on the spatial resolution properties of the reconstructed images. Therefore optimizing the spatial resolution can also be used as a criterion for their optimal selection. Furthermore for scanners utilizing image reconstruction based on spherical symmetric basis functions, the image space PSF could depend upon the selection of the basis function parameters. Image reconstruction on the Ingenuity TF PET/MR is based on spherical symmetric volume elements using Kaiser-Bessel window functions and as such its reconstructed spatial resolution and consequently its image-based PSF could be dependent upon the basis function parameters.

In this work, we experimentally measure the spatial-variant PSF of the Ingenuity TF PET/MR in image space and investigate its spatial resolution properties using a printed point source array technique and a custom made phantom design. We also perform a direct search into the

multidimensional Kaiser-Bessel parameter space to investigate the impact of each parameter on the spatially variant resolution characteristics. Finally, we investigate the resolution characteristics and derive the image space PSF for those basis function parameters which minimize error in the reconstructed images, in order to derive parameters optimizing both error and spatial resolution.

2. THEORY

2.A. Image modeling using spherical symmetric basis functions

As mentioned above, the task of image reconstruction is to approximate the underlying activity distribution by representing it as a superposition of shifted and scaled copies of a basis function (b). During image reconstruction, the scaling factors for each shifted copy of the basis function are calculated in the form of coefficients and stored for visualization. Therefore lets define a three-dimensional grid in space with J uniformly distributed points or grid nodes, each being localized in space by a unique set of x_j, y_j, and z_j coordinates, representing the origin for each shifted basis function and with a sampling frequency of $1/d$. Also for each spherical symmetric basis function b, the amplitude can be considered to be only a function of distance from the origin $\|x - x_j, y - y_j, z - z_j\|$ such that $b = b(\|x - x_j, y - y_j, z - z_j\|)$. Then the reconstructed image can be modelled as

$$f(x, y, z) = \sum_{j=1}^{J} a_j b(\|x - x_j, y - y_j, z - z_j\|), \tag{1}$$

where a_j are the coefficients of each shifted basis function b at node j with its origin at (x_j, y_j, z_j).[20] The difference of using spherical symmetric elements as opposed to cubic is that their shape and size can be freely adjusted to reflect certain properties. Adjacent copies of the basis function are also allowed to overlap in space, with the degree of overlap being a function of the basis function parameters and their sampling distance in the 3D basis function space.

2.B. Three-dimensional Kaiser-Bessel spherical functions

A widely known family of spherical symmetric basis functions, used by the Ingenuity TF PET/MR system for image representation and reconstruction, is the Kaiser-Bessel family of window functions. The use of these multi-parameter basis functions in tomographic image reconstruction was first proposed by Lewitt[21] and further exploited by Matej and Lewitt[23] and can be generally described as

$$b\{m, alpha, r, R\} = \frac{I_m(a\sqrt{1-(R/r)^2})}{I_m} \times (\sqrt{1-(R/r)^2})^m \quad \text{for } 0 \le R \le r, \tag{2}$$

where

$$b\{m, alpha, r, R\} = 0, \quad \text{for } R \ge r$$

with

$$R = \sqrt{(x - x_j)^2 + (y - y_j)^2 + (z - z_j)^2},$$

where m is the order of the function and is a non-negative integer which controls the continuity conditions at the boundaries of the function, alpha is a parameter which controls the shape of the function, r is the function radius, R is the distance from the function origin, and I_m is the modified Bessel function of the mth order. As can be seen, the amplitude of the Bessel function inside the boundaries is a function of many parameters with a bell-shaped radial profile. Looking at the power spectrum of a Kaiser-Bessel function, the relative power and consequently the amplitude, drops to very low values after a certain frequency.[20] Therefore, the function is practically band-limited as opposed to a Gaussian function which is not and will have to be truncated.

2.C. Parameter selection for image representation and reconstruction

The parameter space of the Kaiser-Bessel window function is multidimensional and the choice of parameters will inevitably affect the properties of the reconstructed images. One of the parameters is the order of the function. For $m > 0$, the basis function is continuous with $m - 1$ continuous derivatives, therefore it is desirable to use $m > 1$. However, higher m values create smooth basis functions, with long low amplitude tails, which will impact the computation time in forward and back-projection during reconstruction, without significantly altering the resulted image. Therefore using a 2nd order Kaiser-Bessel basis function provides a good compromise based on the aforementioned constraints.

The basis function radius is another parameter which is of importance and impacts both the computation load as well as the properties of the reconstructed image. It defines the support of the basis and for a given basis sampling distance in the 3D basis function space, controls the degree of overlap between adjacent basis functions. A larger radius results in increased reconstruction time, which often puts a constraint on its selection for practical applications. The alpha parameter on the other hand does not impact the computational load and its selection therefore can be optimized purely based on the properties of the reconstructed images which are desirable. A large alpha parameter results in a smoother transition from the origin to the basis function boundaries, with the amplitude dropping closer to the origin. A small alpha value results in a sharper transition and with the function amplitude dropping at a larger distance from the origin. The difference caused in the basis function amplitude between progressively increasing/decreasing alpha values depends on the order of the function.

Finally, another parameter of importance is the spatial arrangement of the basis functions and the sampling interval between their origins. Although a simple cubic arrangement is most widely used and known in tomographic reconstruction, a body centered cubic grid was found to be more efficient for spherical symmetric basis functions.[24] The sampling distance heavily impacts the computation load, as more nodes

are needed to cover a given image space. For a given basis radius, changing the sampling distance will result in a different overlap and, as such, the absolute blob radius is not always informative. Instead a relative radius, normalized to the basis sampling distance is often used. Consequently, as the basis order is often fixed to $m = 2$, three parameters need to be selected during image reconstruction, based on their impact either on the computational load, or on the properties of the reconstructed images. Although for practical applications both are taken into account, this investigation considers the latter. For a fixed m value, the full width at half maximum as well as tails of the basis function, are solely controlled by the radius and the alpha parameter. Therefore, the signal-to-noise ratio and spatial resolution of the reconstructed images can vary for different values of these parameters. Due to the overlapping between basis functions, one criterion to constrain the parameter selection is to choose parameters which minimize the error by which a uniform image can be represented. This leads to a condition in which the Fourier transform of the basis function needs to have a zero amplitude at multiples of the sampling frequency $1/d$ in the basis function grid. This condition, however, is not exactly satisfied for the Kaiser-Bessel functions, but parameters can be chosen to approximately satisfy the above condition and constrain the image representation and reconstruction error below an acceptable level. Therefore parameters can be chosen so as the 1st, 2nd, or any subsequent zero crossing occurs exactly at a radial distance equal to $1/d$, with the power spectrum of the Fourier transform of the basis function close to zero at other multiples of the sampling frequency.[23] This ensures that fluctuations in the reconstructed image around the true value have the minimum possible impact on the desired properties and subsequent analysis of the images, given that the condition for zero crossing at all sampling frequency multiples cannot be fully met for the Bessel basis function. To be able to satisfy the above condition, the three parameters become correlated and the normalized blob radius is given as

$$r/d = \frac{\sqrt{a^2 + u_i^2}}{2\pi}, \tag{3}$$

where u_i is the ith zero of the three-dimensional Bessel function $J_{m+3/2}$ and can be taken from lookup tables. Parameters which satisfy this equation result in an error below an acceptable limit when reconstructing a uniform region. However, the set of parameters satisfying the above equation and are able to represent a smooth image with the minimum degree of error are not likely to optimize another important property which is the spatial resolution. Consequently, a direct search through the multidimensional Kaiser-Bessel parameter space could be performed, focusing on the impact of the parameters on the spatial resolution rather than minimum error.[23]

2.D. Image reconstruction using overlapping and spherical symmetric basis functions

Image reconstruction using spherical symmetric basis functions, as demonstrated by Stute and Comtat,[22] can be considered as an image space resolution modeling image reconstruction in basis function coefficient space, using the basis density function as the resolution kernel, followed by an image space convolution with the basis function. For ordered subsets expectation maximization image reconstruction, this equates to

$$\lambda_j^{(n+1,k)} = \frac{\lambda_j^{(n,k)}}{\sum\limits_{i \in S_{N+1}} p_{ij}} \sum_{i \in S_{N+1}} \frac{p_{ij} \mathrm{m}_i}{\sum\limits_{j'} p_{ij'} \lambda_{j'}^{(n,k)} + \eta_i}, \tag{4}$$

where for a given LOR i intercepting the spherical basis function localized at (x_j, y_j, z_j) $p_{ij} = \iiint dxdydz b(R)$ followed by a convolution with $b(R)$. As pointed out by Stute and Comtat[22] the scanner's PSF can also be used as a basis function, provided of course that an initial voxel reconstruction is available to derive the voxel-based image space PSF. However, in such an event, and in contrast to using Kaiser Bessel functions where the parameters can be optimally selected, the mathematical criteria needed for optimally superimposing basis functions with minimum error, are most likely not satisfied due to the PSF having a fixed density function.[23] Therefore, for scanners using spherical symmetric Kaiser Bessel basis functions and in the absence of a voxel-based reconstruction, the scanner's resolution could vary significantly for different arbitrarily defined basis function parameters. This is particularly true for parameters corresponding to basis functions with FWHM larger than that of the scanner's PSF, in which case apart from overshoot, a deterioration in the reconstructed resolution could also potentially occur. Therefore, parameters could be optimized based on spatial resolution rather than error to avoid such effects. However, with each scanner having a different PSF, parameter optimization is empirical and scanner dependent. Furthermore, deriving the scanner's image-based PSF using an image reconstruction based on Kaiser-Bessel functions, could result in the image-based PSF depending on the basis function parameter selection. Alternatively and in order to satisfy the conditions in Fourier space for minimum error, spatial resolution optimization could be done for those parameters which satisfy Eq. (3). Hence parameters which simultaneously optimize error and spatial resolution during image reconstruction can be selected, in order to derive the scanner's image space PSF.

3. MATERIALS AND METHODS

3.A. The Ingenuity time-of-flight PET/MRI scanner

The Philips Ingenuity TF PET/MR system is a state-of-the-art recently commercialized hybrid imaging system, which combines the Gemini TF PET and the Achieva 3T X-series MRI systems. The system provides sequential imaging between the two scanners using a rotating patient handling system, allowing fused images to be obtained similar to a standard PET/CT system. A number of features on the PET system had to be redesigned in order to avoid mutual interference between the two systems. To avoid electromagnetic interference due to the stringent requirements when operating inside the magnet room, some of the PET electronics,

including power and signal wires, are located in the MR equipment room. To avoid interference from the fringe magnetic field on the PET detector PMTs, shielding was introduced on the MRI side, while the PMTs were reorientated parallel to the magnetic field. The PET system has 28 336 4 × 4 × 22 mm LYSO crystals arranged in 28 modules providing ∼12% energy resolution and ∼580 ps timing resolution, enabling the usage of TOF information. Image modeling is done using Kaiser-Bessel basis functions while image reconstruction is performed in list-mode and a relaxed OSEM algorithm is provided allowing TOF and non-TOF data to be reconstructed.[25] Attenuation data are provided using a three-class (air, lung, soft tissue) automatic segmentation while scatter estimation is based on TOF-dependent single scatter simulation.

3.B. Point source production and optimization

To produce the point source array, a standard HP printer was used to print multiple radioactive Fluorine-18 point sources on an A4 paper using a predefined template array drawn on Microsoft publisher. Ink (∼0.3 ml) was mixed with fluorine-18 (∼0.1 ml) and the solution was injected into a modified cartridge via a syringe. An array of 12 × 7 sources in the radial and axial direction, respectively, was printed. A conservative 2.5 cm point source spacing was used both in the axial and radial direction, to avoid any overlap of the reconstructed PSFs. The point sources were 1 mm in diameter and the array covered half the radial FOV (0…27.5 cm) and almost the entire axial FOV (−7.5…7.5 cm). To boost the activity printed, the paper was reprinted three times ensuring activity deposition at the same position in each reprint. Since the paper has not got sufficient material for the positrons to annihilate, a Perspex phantom was used for that purpose. A tissue equivalent phantom consisting of two Perspex sheets (3 mm thick/sheet), between which the array was placed, was used for positioning and to provide annihilating material (Fig. 2).

3.C. Positioning, aligning, and scanning the point source array

To place the Perspex sheets in the FOV and allow movements in different directions for precise positioning of the sources, the phantom holder used for daily QC of the PET scanner was modified to accommodate the point source array. Holes were drilled in 2 cm intervals at the top bracket of the point source QC holder and the Perspex sheets were screwed to place, extending from the center towards the end of the radial FOV. Accurate positioning of the array was assisted by the scanner's laser system which although not used for direct alignment due to an offset with respect to the scanner's axis and the true PET FOV, provided a fixed reference frame. Multiple test scans of the point source array were acquired and reconstructed to locate the center of the FOV and subsequent adjustments were done with respect to the laser system. Printed guide-lines on the point source array helped with the alignment with respect to the reference laser lines. Once in place and with the MR magnet on, PET data were acquired in PET only mode for 120 min (no MR data were acquired), to enable high counting statistics data to be collected (∼100 M prompts).

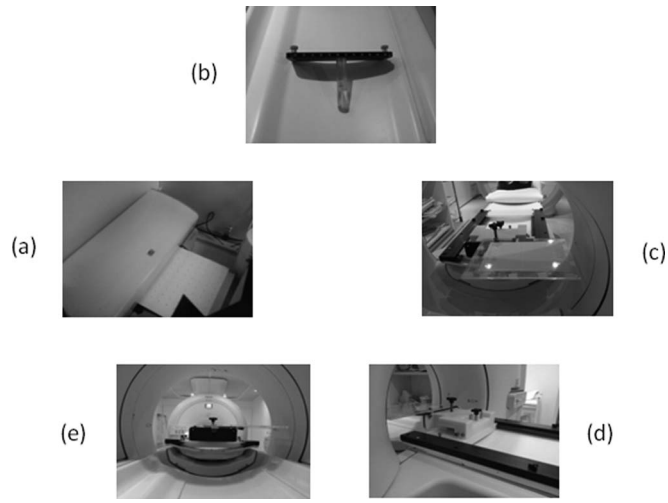

FIG. 2. A printer was used to produce the point source array (a). Holes were drilled on the top of the QC point source holder at 2 cm intervals (b) and the Perspex sheets with the point source array were screwed in place (c). The assembly was then attached on the phantom holder which was subsequently attached on the patient handling system with the help of railings (d). The array was positioned horizontally, extending from the center towards the edge of the radial FOV (e).

3.D. Image reconstruction and PSF modeling

Since the data were acquired in PET only mode, no attenuation correction was used, which is a reasonable assumption since the Perspex sheets result in minimal attenuation. Furthermore, since an attenuation map was not readily available, scatter correction was not performed during the reconstruction. The PSF data were reconstructed using a list-mode time-of-flight OSEM algorithm available on the system.[25] To avoid any additional blurring from lack of convergence, test data were reconstructed using various iterations to establish the point were no further improvements could be seen on the spatial resolution. In the rest of the analysis and following this iteration optimization based on the rate of change in the FWHM, seven iterations were used for all point source data. Images were reconstructed on a 288 × 288 × 90 grid for visualization and post-reconstruction analysis with a 2 × 2 × 2 mm voxel.

To evaluate the impact of Kaiser-Bessel basis function parameters on the spatial resolution and the image-based PSF, three parameters were varied during reconstruction. Two different parameter selection schemes were used. In the first scheme, basis function parameters were systematically varied over a predetermined range of values. First, 13 logarithmically spaced values for the blob radius were evaluated (r/d = [1, 1.1, 1.21, 1.33, 1.47, 1.62, 1.78, 1.97, 2.17, 2.39, 2.63, 2.90, and 3.19]) normalized to the basis function interval (d). For each blob radius, ten alpha parameters were evaluated (a = [0.4, 0.53, 1.30, 2.36, 3.18, 4.27, 5.75, 7.74, 10.41, 14]). Finally, the blob sampling interval was evaluated using two

TABLE I. Parameter selection scheme satisfying criteria for minimum error of a uniform function based on the zero crossing of the Fourier transform of the Kaiser-Bessel basis function. Parameters are estimated for the 1st, 2nd, and 3rd zero crossing of the power spectrum at a distance equal to the lattice sampling frequency (1/d).

Alpha	r (1st zero crossing)	r (2nd zero crossing)	R (3rd zero crossing)
0.4000	1.1349	1.6903	2.2219
0.5379	1.1364	1.6913	2.2227
1.3084	1.1527	1.7023	2.2311
2.3664	1.1962	1.7321	2.2539
3.1825	1.2450	1.7661	2.2801
4.2799	1.3286	1.8260	2.3269
5.7559	1.4679	1.9297	2.4091
7.7408	1.6908	2.1043	2.5511
10.4101	2.0329	2.3878	2.7896
14.0000	2.5370	2.8294	3.1758

basis function sampling schemes (d = [1.0188 and 2.0375]). In the second scheme, parameters were chosen so as to satisfy Eq. (3), which is a prerequisite for optimizing/minimizing error in representing a uniform function. Then using a fixed sampling scheme (d = 1.0188) and the same alpha parameters as in the first parameter selection scheme (a = [0.4, 0.53, 1.30, 2.36, 3.18, 4.27, 5.75, 7.74, 10.41, 14]), the basis function radius was determined for each alpha value from Eq. (3). To cover all possible combinations, parameters were derived for the 1st (u_1 = 6.988), 2nd (u_2 = 10.417), and 3rd (u_3 = 13.698) zero crossing. The combination of parameters used in the 2nd parameter selection scheme, based on Eq. (3) and using the aforementioned alpha and sampling parameters, are summarized in Table I.

The reconstructed PSF data were fitted in image space using a Gaussian mixture model of two 3D distributions estimating 13 parameters (standard deviation and mean with axial, radial, and tangential components for each Gaussian with a weighting parameter between them).[14] Parametric maps representing the axial and radial spatial variation of each PSF fitted parameter, as well as FWHM, were generated for each blob parameter combination in the 3D blob parameter space. In the analysis that follows, we used FWHM as an overall index of interest in evaluating the image space PSF with individual fitted parameters probing certain aspects of the PSF, such as shape and asymmetry.

3.E. Qualitative evaluation

To qualitative evaluate the impact of the different basis function parameters, the NEMA image quality body phantom, filled with fluorine-18 and with a 5:1 sphere to background ratio was scanned on the Ingenuity PET/MR. Data were acquired for 10 min collecting ~100 M prompt events and were reconstructed with a list-mode time-of-flight OSEM algorithm (7 iterations—33 subsets). Representative parameter combinations were used, taking into account the spatial resolution based parameter optimization as well as parameter combinations derived from Eq. (3). Furthermore, a clinical brain study was also used for qualitative evaluation. The patient was injected with ~265 MBq of [^{18}F]-FDG, followed by a 10 min data acquisition, collecting ~140 M prompts. Similar to the phantom study, a list-mode time-of-flight OSEM algorithm (7 iterations—33 subsets) was used along with representative basis function parameters.

4. RESULTS

4.A. PSF variation under spatial transformations

Transverse and horizontal reconstructed images through the point source array are shown in Fig. 3 for standard basis function parameters (r = 1.0188, alpha = 1.3084, d = 1.0188). From a qualitative evaluation of the data, the radial elongation of the kernels towards the edge of the radial FOV is easily discernible. In the center of the FOV, the PSFs appear to be symmetric and become progressively elongated at increased radial distance. Looking at the axial dependency, no qualitative difference can be seen between the reconstructed PSFs at the 7 axial positions. Following reconstruction of the data and post-reconstruction PSF model fitting as outlined in the methodology, model parameters and the FWHM were estimated for each of the fitted kernels. Parametric images of the radial, tangential and axial FWHM corresponding to the reconstructed point source data of Fig. 3 are shown in Fig. 4(a). Each voxel in these spatial resolution parametric maps corresponds to a single point source and covers a physical sampling distance of 2.5 cm, equal to the sampling distance between the point sources in the array. The quantitative data confirm the findings from the visual inspection of the reconstructed data. The radial FWHM was found to vary from ~4 mm in the center of the radial FOV up to ~6.6 mm at a radial distance of 27.5 cm and close to the edge of the reconstructed radial FOV. Looking at the tangential and axial FWHM, it appears that the axial and tangential components of the PSF are invariant under radial transformations, with a FWHM of ~4 mm. Looking at the axial dependency of the radial, tangential, and axial components of the PSF, they all appear to be invariant under axial transformations, with

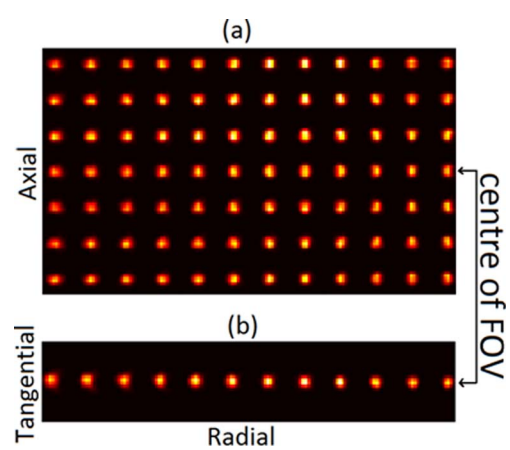

FIG. 3. (a) Horizontal and (b) transaxial sections through the 3D reconstructed image (r = 1.0188, alpha = 1.3084, d = 1.0188). Towards the edge of the radial FOV, the kernels become elongated from parallax error effects.

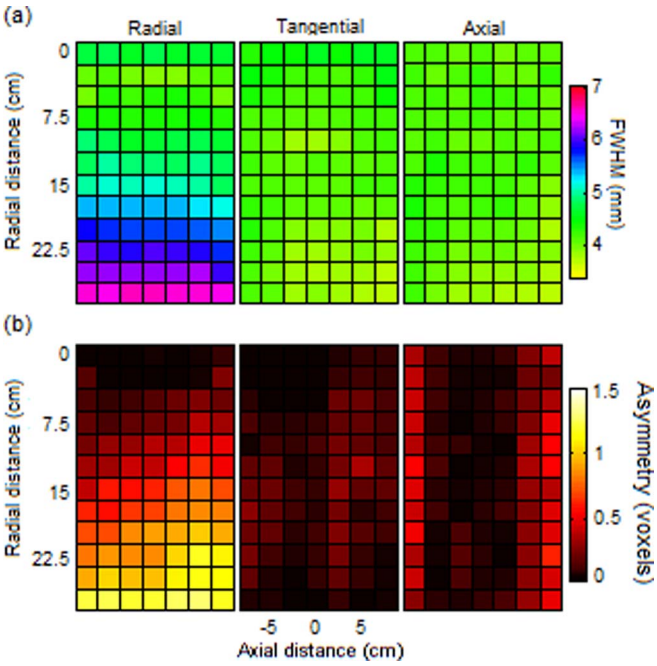

FIG. 4. Parametric maps for standard blob parameters (r/d = 1, alpha = 1.3084, d = 1.0188) of radial, tangential, and axial (a) FWHM and (b) asymmetry. Asymmetry is estimated as the spatial difference between the respective means of the two Gaussian distributions used to fit the reconstructed kernels.

minimum variation in the FWHM across the axial FOV. One aspect of the scanner's spatially variant PSF is the parallax error induced radial elongation which causes the PSF to become asymmetric away from the scanner's axis. Rather than looking at the FWHM, a better insight can be obtained by directly probing this asymmetry. In Fig. 4(b) the spatial variation of the radial, tangential, and axial PSF asymmetry is shown as a parametric image, with the asymmetry given as the spatial difference between the corresponding fitted means of the 2 Gaussian distributions. As expected, a substantial asymmetry is observed in the radial direction. In the center of the radial FOV, no asymmetry is observed as the PSF approximates a Gaussian distribution and the means of the two Gaussians, used to model the reconstructed kernels, coincide in space. At increased radial distance the radial asymmetry is progressively increased up to ∼1.5 voxels (3 mm) as the means of the two Gaussian distributions are stretched further apart to model the asymmetric PSF. In the tangential direction, no significant asymmetry is observed throughout the FOV. However, a small axial asymmetry was observed towards the edge of the axial FOV (∼0.5 voxels), which appears to be symmetric with respect to the center of the axial FOV and could be caused by axial parallax error effects. This asymmetry is not creating any visible deterioration in the axial FWHM towards the edge of the axial FOV as seen in Fig. 4(a), as it is relatively small and potentially only noticeable if using a full width at tenth maximum index (FWTM).

4.B. PSF variation under different basis function parameters

Following evaluation of the scanner's variable image space PSF and resolution characteristics under spatial transformations using standard basis function parameters, a systematic evaluation over a range of basis function parameters was performed to assess their impact on the aforementioned scanner attributes. In Fig. 5, parametric images of radial, tangential, and axial FWHM are compared for two largely different basis function radius (r/d) and a small alpha parameter (alpha = 1.3084) using a sampling distance of d = 1.0188. Using a relatively small alpha value, which allows the basis function to still have a high amplitude close to the boundaries, and going from a small radius to a large radius, the reconstructed PSF significantly broadens. As can be seen, both the tangential and the axial FWHM uniformly deteriorates from ∼4 to ∼5.5 mm. However, the radial resolution does not follow the same trend and deteriorates as a function of the distance from the scanner's axis. In the center of the FOV, the deterioration is similar to what is seen in the tangential and axial direction. Moving progressively away from the center of the radial FOV, where the resolution naturally deteriorates due to parallax effects, the basis function induced deterioration from using a larger radius is progressively reduced. At the very end of the FOV, no visible resolution degradation is caused by increasing the basis radius. Therefore, due to the nonuniform way the resolution is affected from the basis radius, owning to the parallax error induced resolution gradient, the overall FWHM although degrading, becomes less variant. The spatial resolution can be seen for all 13 different basis function radii in Fig. 6(a) were the radial, tangential, and axial FWHM averaged across the seven axial positions is plotted as a function of radial distance. Using a radius of up to 1.9708, no significant

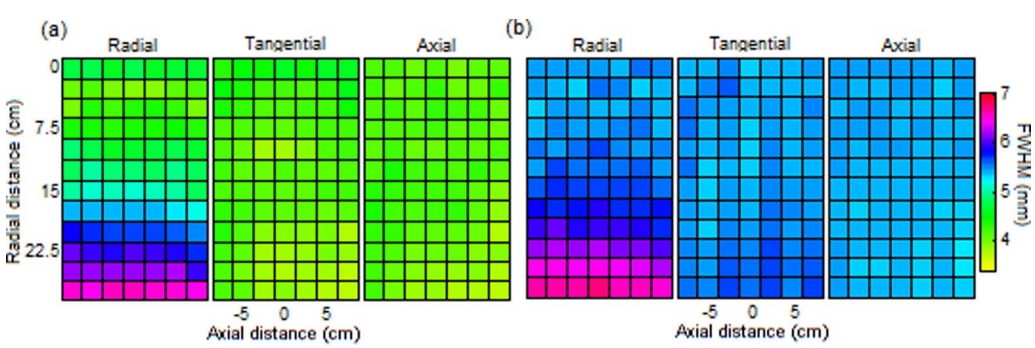

FIG. 5. Parametric maps of radial, tangential, and axial FWHM for alpha = 1.3084 and for blob radius (a) r/d = 1 and (b) r/d = 3.19 (d = 1.0188).

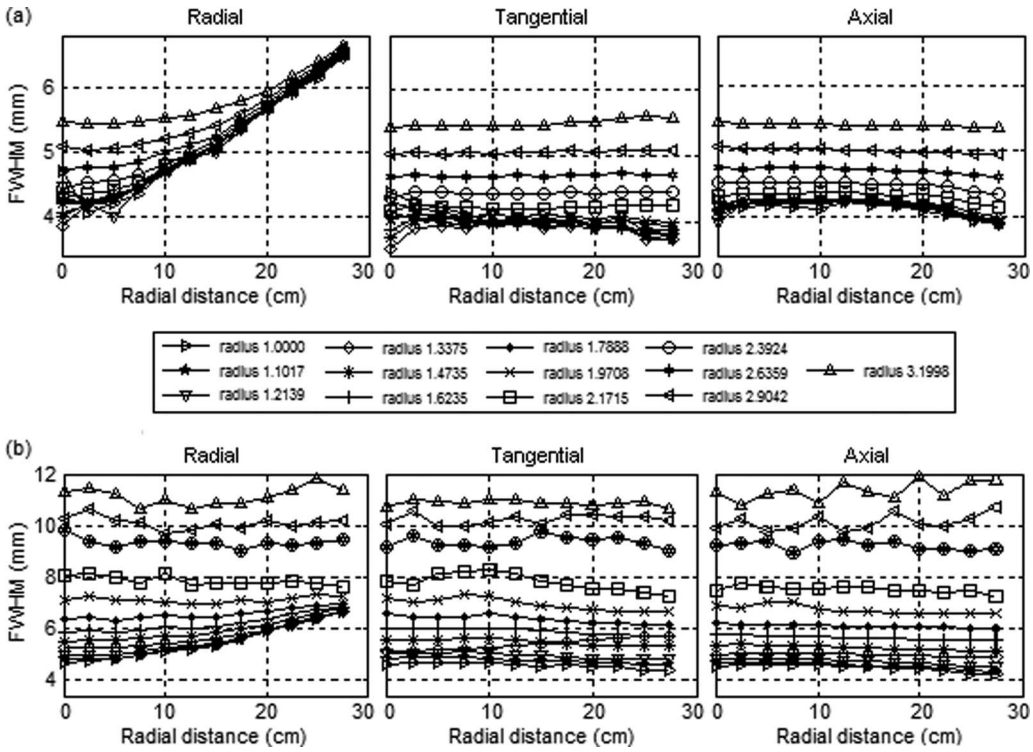

FIG. 6. Radial, tangential, and axial FWHM as a function of radial distance (average across the seven axial positions) for alpha = 1.3084 and for 13 different basis function radii using a sampling distance of (a) d = 1.0188 and (b) d = 2.035.

difference is seen in the resolution. For higher values, the FWHM starts to deteriorate. In the radial FWHM and for a radius of 3.1998, the resolution gradient from the center to the edge of the FOV has been reduced to less than 1 mm, while in the axial and tangential direction, the resolution deteriorates uniformly and in a similar way across the FOV. The same analysis but using double the sampling distance (d = 2.035) and physical basis function radius (normalized radius is the same as it is given as their ratio) is shown in Fig. 6(b). The resolution degradation pattern is kept the same, though now degradation starts from a smaller radius (r/d = 1.21) despite the normalized radius being the same. Above a radius of r/d = 1.97, both radial, tangential, and axial resolution becomes truly spatially invariant across the FOV and close to ~8 mm while it reaches ~11.3 mm at the peak radius (r/d = 3.19).

On the other hand, using a relatively large alpha value (alpha = 14), which allows the basis function's amplitude to drop rapidly away from the origin with long low amplitude tails, and going from a small radius to a large radius, the reconstructed PSF stays largely unchanged as seen in Fig. 7. It can also be seen that when a small radius is used, the resolution parametric maps appear noisy with sudden variations. This could be attributed to the fact that a combination of a small radius with a large alpha, both contributing to a Bessel function with small FWHM and poor basis overlap, is far away from the optimum parameters satisfying Eq. (3). Therefore nonuniformities from improper overlap between the basis functions will propagate and manifest in the reconstructed point sources and consequently in the PSF fitting and spatial resolution estimation. Going to the other extreme at a large radius (r = 3.19), even though the alpha is large, the resolution map appears very uniform, while in the radial direction the FWHM is transitioning smoothly due to parallax error with no sudden changes.

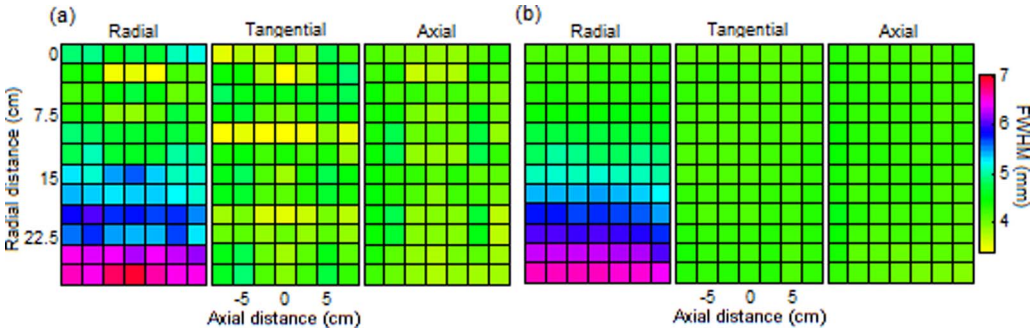

FIG. 7. Parametric maps of radial, tangential, and axial FWHM for alpha = 10.4101 and for blob radius (a) r/d = 1 and (b) r/d = 3.19 (d = 1.0188).

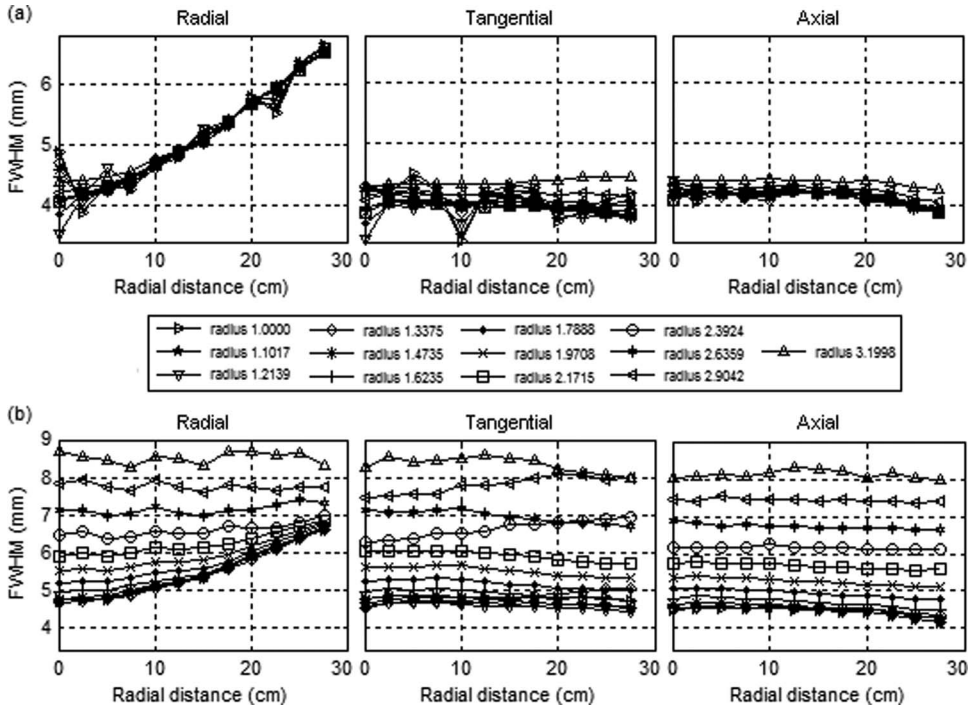

FIG. 8. Radial, tangential, and axial FWHM as a function of radial distance (average across the seven axial positions) for alpha = 10.4101 and for 13 different basis function radii using a sampling distance of (a) d = 1.0188 and (b) d = 2.035.

Again and in a similar way to Fig. 6(a), spatial resolution can be seen for all 13 different basis function radius values in Fig. 8(a) were the radial, tangential, and axial FWHM averaged across the seven axial positions is plotted as a function of radial distance. As alpha is large (alpha = 14), resulting in a fast drop in the basis function amplitude away from the origin, even if the radius is large, no significant difference is seen in the spatial resolution. However, as previously mentioned, data reconstructed with a small radius suffer from sudden variations in the resolution mainly due to nonuniformities in the reconstructed PSF image. When a double sampling distance and physical radius is used, it inevitably leads to a broadening of the reconstructed PSF kernels and resolution degradation as seen in Fig. 8(b). Degradation starts at a radius r/d = 1.62 with the spatial resolution becoming spatial invariant at a radius r/d = 2.63. At the peak radius (r/d = 3.19), resolution peaks at ~8.8 mm which is lower compared to the ~11.3 mm seen in Fig. 6(b) due to the difference in the alpha parameter.

To assess the impact of alpha on spatial resolution, the radial, tangential, and axial FWHM averaged across the seven axial positions is plotted for all 10 alpha values (d = 1.088). Data are shown both using a small radius (r/d = 1.47) and a large radius (r/d = 3.19) (Fig. 9). For a small basis function radius, no difference is observed between the different alpha parameters. When a large radius is used, the impact of the alpha parameter becomes more prominent with the axial and tangential resolution ranging from ~4 to ~5.7 mm uniformly throughout the FOV. Similar resolution degradation is observed in the radial FWHM at the center of the radial FOV, while at the edge of the FOV no resolution difference is seen amongst the different alpha values.

A clearer picture of the impact of each of the three parameters on the radial resolution, which is the only to vary under spatial transformations, can be seen in Fig. 10. When a large alpha value is used, the image space PSF and consequently spatial resolution, remains largely unchanged throughout the FOV. Under a small alpha value, spatial resolution starts to degrade in the center of the radial FOV at a certain radius and approaches the resolution at the edge of the FOV which remains unchanged. Using double the sampling distance (d = 2.0375), the radial component of the PSF becomes spatially invariant as well (similar to the axial and tangential), irrespective of the alpha value as seen in Fig. 10, with the difference between different alpha values being the basis function radius at which it occurs.

One of the incentives of using a double mixture model to model the PSF, apart from being able to account for asymmetry, is that the PSF may not be normally distributed even in the center of the FOV. The 1st component can model the main fast decaying part of the PSF while the 2nd component can model the slowly decaying tails, with their proportion varying as a function of the distance from the center of the FOV and adding up to unity. Therefore, as the radial component of the PSF becomes radially invariant under certain basis function parameters, the proportion between the two Gaussians that model the PSF should also change. This can be seen in Fig. 11 where the proportion of the 1st Gaussian is shown as a parametric image for six different radii (r/d) and two extreme alpha values. As seen in Fig. 11(a)(i), which corresponds to a combination of parameters that do not degrade resolution, the proportion of the 1st Gaussian in the center of the radial FOV is ~75% (with the 2nd Gaussian accounting for the other 25%) while it is reduced to ~65% at the edge of the FOV due

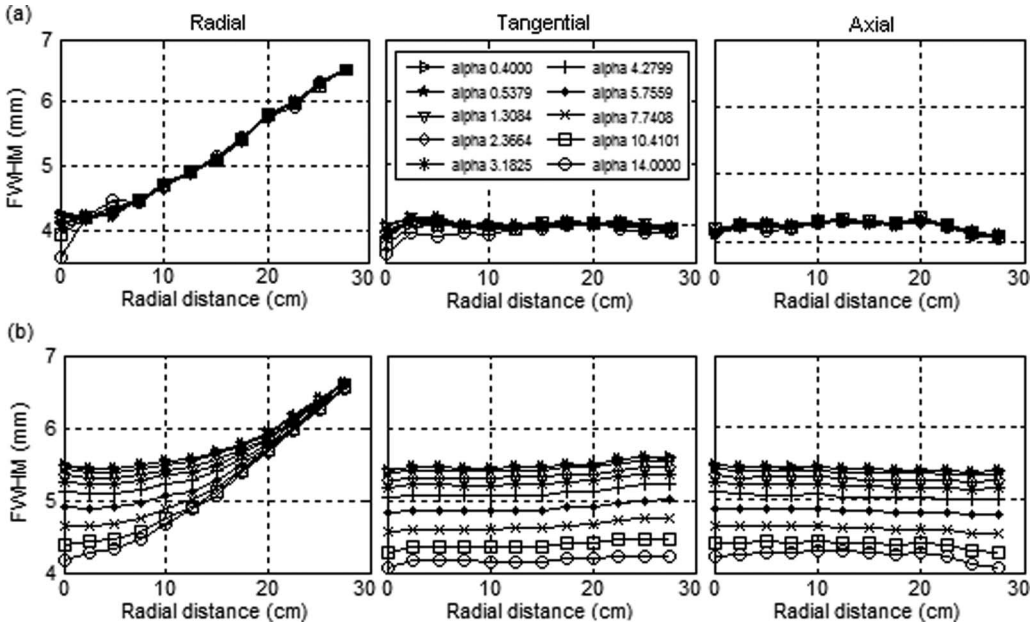

FIG. 9. Radial, tangential, and axial FWHM as a function of radial distance (average across the seven axial positions) for ten different alpha values using a radius of (a) r/d = 1.4735 and (b) r/d = 3.1998 (d = 1.0188).

to the larger tails which are modeled by the 2nd Gaussian. Increasing the radius of the basis function as seen before, results in the radial component of the image space PSF to become less variant under radial transformations. This has an impact on the shape of the PSF as can be seen in Fig. 11, with the percentage of the 1st Gaussian increasing as the basis function radius increases and approaching unity. This signifies that the PSF becomes more symmetric and could even be modeled by a single Gaussian. Furthermore, the percentage varies less as a function of radial distance, as the radial component becomes less spatially variant. Similar behavior is seen for the two alpha values with the proportion changing significantly less when using a large alpha.

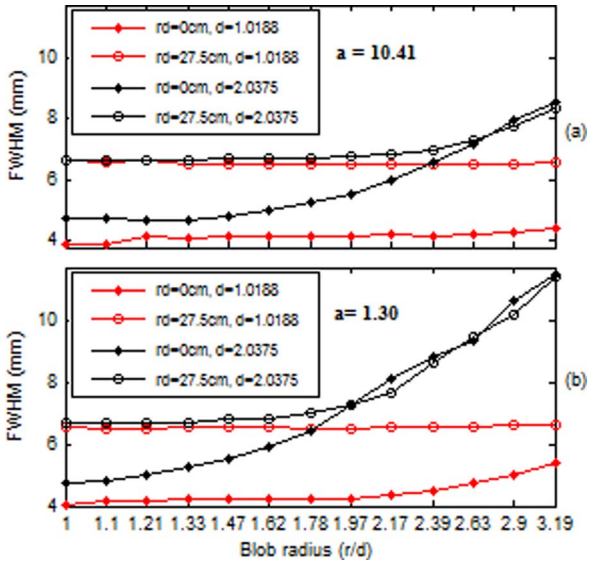

FIG. 10. Plots of radial FWHM at the center (rd = 0 cm) and edge (rd = 27.5 cm) of the radial FOV (average across the seven axial positions) for two basis function sampling distances (d = 1.0188 and d = 2.0375) as a function of blob radius. Plots are shown using two shape parameters a = 10.41 (a) and a = 1.30 (b).

Based on the results presented using a combination of basis function parameters, the image space PSF could become spatially invariant. However, the overall reconstructed resolution is degraded and gradually dominated by the basis function's FWHM. Due to the parallax error induced resolution degradation at the edge of the radial FOV, the degradation caused by the basis function FWHM is first noticeable in the center of the FOV. Therefore, the basis function parameters can easily be optimized to avoid any resolution degradation by looking at Fig. 12, where the FWHM at the center of the FOV (averaged across the seven axial positions) is visualized for all the alpha parameters and radii (d = 1.0188). Based on the parametric image shown in Fig. 12(a), contour plots can be generated similar to those used by Matej and Lewitt.[23] As can be seen from the contour plots, the contour line corresponding to 4.2 mm can be used as a threshold, with parameter combinations on the right side degrading spatial resolution. However, parameters close to the upper left side of the graph, corresponding to a small radius and a large alpha, although not degrading resolution, generate images with nonuniform resolution characteristics. This can be seen when looking at the tangential resolution contour plot as well as Fig. 7(a). Therefore, it is desirable to investigate whether parameters which satisfy Eq. (3) for minimum error could also maximize spatial resolution, thus achieving a double optimization of error and resolution at the same time. Such an optimization is shown in Fig. 13 where the radial, tangential, and axial FWHM at the center of the FOV (averaged across the seven axial positions) is plotted for basis function parameters which satisfy the condition for minimum error imposed by Eq. (3). Results are shown based on the first three zero crossings of the Fourier

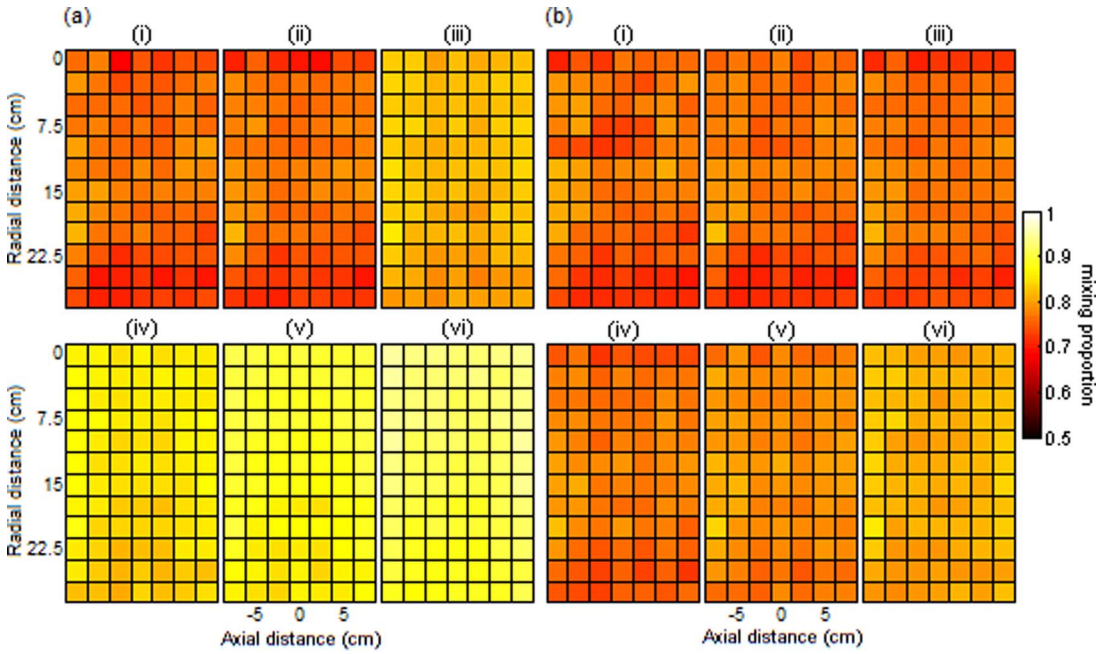

FIG. 11. Parametric maps of the mixing proportion of the 1st Gaussian distribution (proportion of both Gaussian distributions add to unity) for six different basis function radii [r/d = 1.21 (i), 1.62 (ii), 2.17 (iii), 2.63 (iv), 2.90 (v), and 3.19 (vi)] (d = 1.0188) and for (a) alpha = 1.3084 and (b) alpha = 10.4101. As the radius increases, the proportion of the 1st Gaussian, which models the fast decaying part of the PSF, also increases and approaches unity, suggesting a more Gaussian-like distribution. Furthermore the proportion becomes less variant as a function of radial distance.

transform of the basis function. As can be seen, combination of parameters belonging to the first two crossings generates Bessel basis functions, which when used during image reconstruction, generate a PSF with optimum spatial resolution. Therefore, points in the first two crossings satisfy both the spatial resolution and minimum error criteria. However, parameter combinations in the 3rd zero crossing degrade spatial resolution although they provide minimum error when reconstructing a uniform region. What is also observed is that parameters close to the upper left side of the contour graph in Fig. 12, corresponding to a small radius and a large alpha and which result in sudden changes in spatial resolution in the FOV, are away from the first hyperbola, resulting in substantial error in the reconstructed images and therefore the

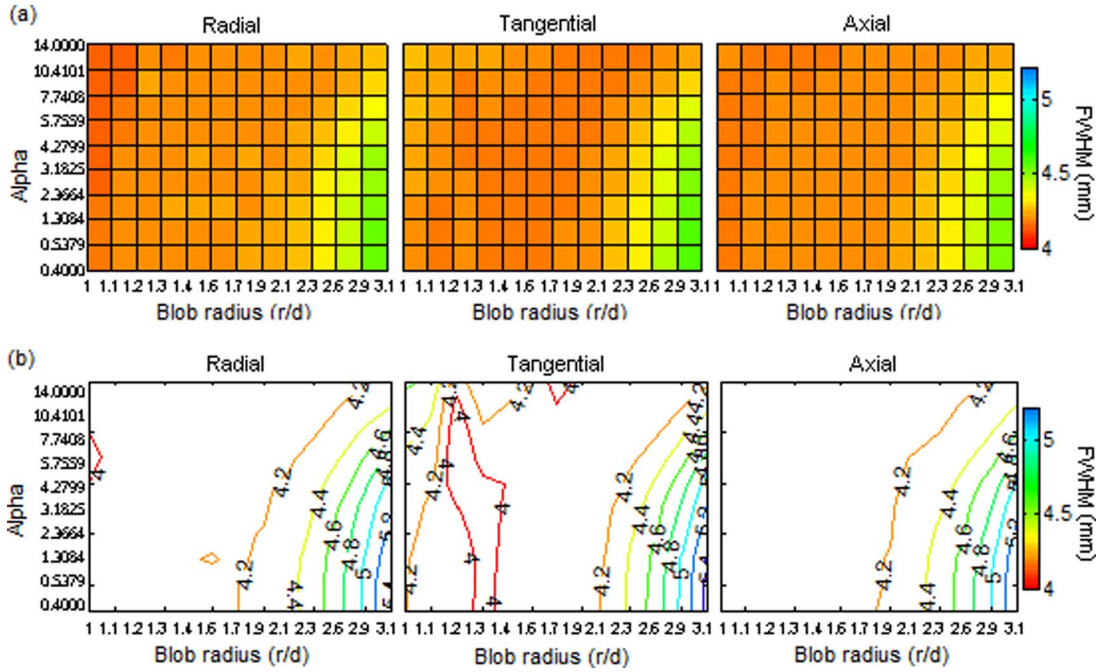

FIG. 12. (a) Parametric maps of radial, tangential, and axial FWHM at the center of the radial FOV (average across the seven axial positions) for ten basis function alpha values and 13 basis function radii and (b) the corresponding contour graphs with contour lines at 0.2 mm increments.

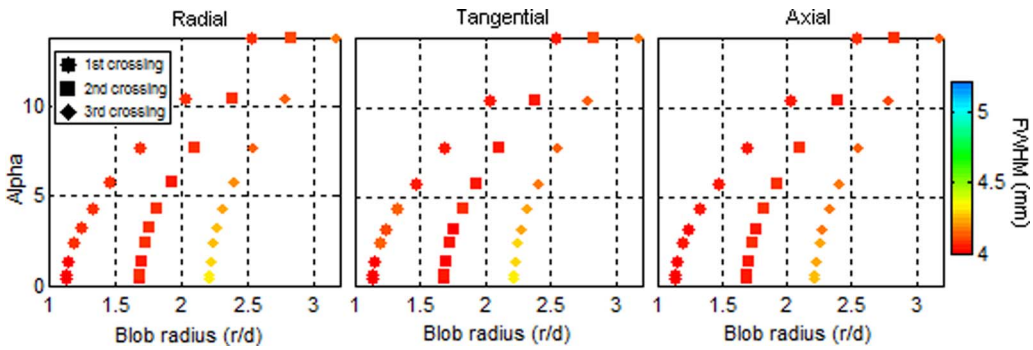

FIG. 13. Radial, tangential, and axial FWHM at the center of the radial FOV (average across the seven axial positions) for 30 combinations of alpha parameter and radii which satisfy the condition for representing a uniform function with error below a reasonable limit as dictated by Eq. (3). Parameter combinations corresponding to the first three zero crossings of the Fourier transform of the basis function at a distance equal to 1/d are shown. Spatial resolution is optimum for parameter combinations belonging to the first two crossings and starts to degrade for parameters belonging to the 3rd crossing.

reconstructed PSF.[23] If we then restrict parameter selection in the first two zero crossings, a smaller error is achieved using a higher radius, with a larger alpha (see Fig. 2 from Matej and Lewitt[23]) as resolution is pretty much unchanged for parameters in the first 2 hyperbolas. The parameter selection could be further restricted by selecting parameters which generate basis functions with the largest possible FWHM and closer to the scanner's PSF, for maximizing the variance improvements achieved by using spherical symmetric basis functions. An image space PSF based on a voxel reconstruction is then needed for that purpose if available, to compare the different basis density functions against it.

Based on the spatial resolution parameter optimization, representative combination of parameters were used on the image quality phantom dataset as seen in Fig. 14. Although when using parameters resulting in a basis function with a small FWHM leads to optimum resolution in the reconstructed image, image nonuniformities appear in the image as parameters are not satisfying the minimum error criteria. In extreme cases, inadequate overlap could lead to severe image artifacts as can be seen in Fig. 14(a). On the other hand, using parameters resulting in a basis function with a large FWHM leads to degraded spatial resolution with potential Gibbs artifacts as shown in Fig. 14(c). Selecting parameters based on the minimum error criteria results in reduced image nonuniformity and noise, however, reconstructed spatial resolution could be far from the optimum. This is confirmed in Fig. 15 where the 1D profile through the smallest phantom sphere reveals that using the optimum parameters for minimum error results in a small degradation of the spatial resolution.

Finally a clinical [^{18}F]-FDG brain study was also used to qualitatively evaluate representative parameter combinations (Fig. 16). Similarly to the image quality phantom, when parameters resulting in erroneous overlap are used, severe artifacts appear in the reconstructed PET images. On the other extreme end, images appear substantially blurred when a basis function with a large radius and a small alpha parameter is used. Images reconstructed with the same (r/d) but a larger (d) parameter, appear to be substantially more blurred which is in accordance to what was observed in Fig. 10.

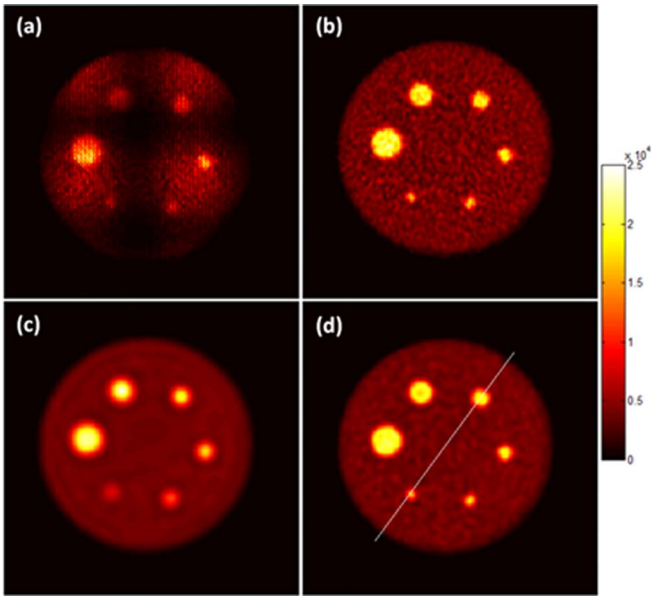

FIG. 14. Representative slice of the NEMA image quality phantom with a 5:1 sphere-to-background ratio used to evaluate representative blob parameters. Data were reconstructed using r/d = 0.5, a = 10.4101 (a), r/d = 1, a = 10.4101 (b), r/d = 3.19, a = 1.3084 (c), representing extreme parameter combinations with a small (a) and (b) and large (c) FWHM in the corresponding blob density function, as well as using r/d = 1.9975, a = 10.4101 (d) with parameters satisfying the minimum error criteria (d = 2.0375) [Eq. (3)].

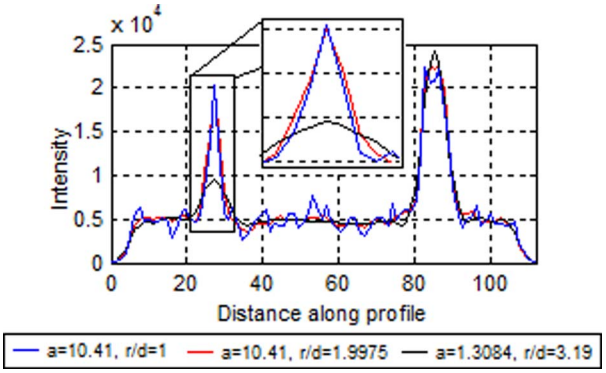

FIG. 15. 1D profile plotted for three images [Figs. 14(b)–14(d)] along the line shown in Fig. 14(d) of the reconstructed image quality phantom.

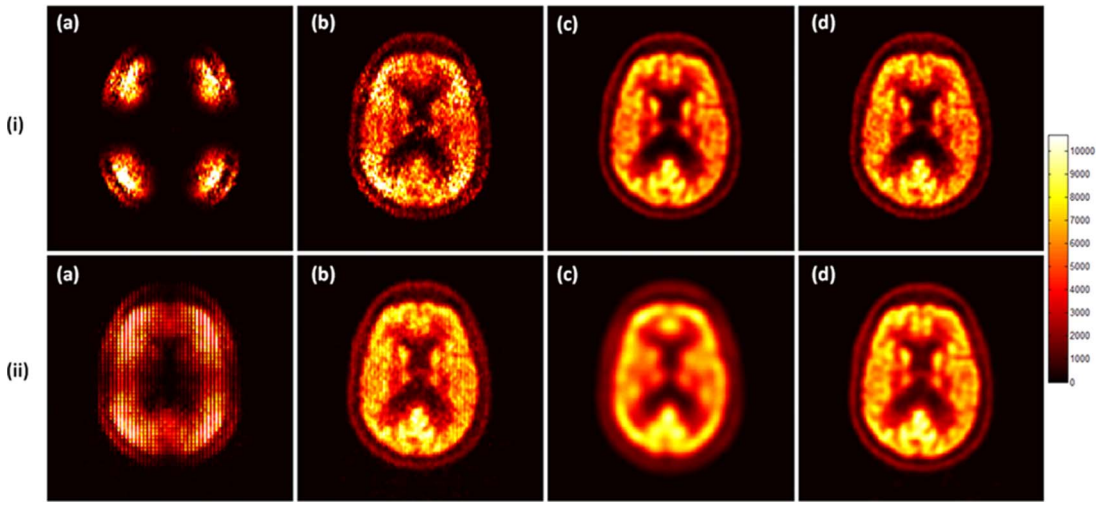

FIG. 16. Reconstructed images of a clinical [^{18}F]-FDG brain study for both d = 1.0188 (i) and d = 2.0375 (ii) with r/d = 0.5, a = 10.4101 (a), r/d = 1, a = 10.4101 (b), r/d = 3.19, a = 1.3084 (c), representing extreme parameter combinations with a small (a) and (b) and large (c) FWHM in the corresponding blob density function, as well as using r/d = 2.3878, a = 10.4101 (d)-(i) and r/d = 1.9975, a = 10.4101 (d)-(ii) with parameters satisfying the minimum error criteria [Eq. (3)]. Parameters in (d)-(i) result also in optimum resolution as can be seen from Fig. 13, something that is not true in (d)-(ii) as spatial resolution has already started to degrade due to the larger (d) parameter used.

5. DISCUSSION

In this work, we aimed at measuring the image-based PSF on the Ingenuity TF PET/MRI scanner to portray the system's spatial resolution characteristics and to derive the spatially variant kernels for potential utilization within a resolution modeling image reconstruction algorithm. However, as opposed to other systems which traditionally use cubic nonoverlapping basis functions for image representation, the system in reference is using a more unconventional basis function implementation, based on spherical symmetric and overlapping volume elements. In the absence of a voxel-based reconstruction, this poses an added complication when deriving the system's PSF in image space due to the multitude of basis function parameters which could arbitrarily and freely be defined and are intrinsic part of image reconstruction. Their selection then inevitably influences the properties of the reconstructed images, and amongst them spatial resolution. Thus we addressed both the image space PSF measurements and the basis function parameter optimization as a unified problem. Previous investigations mainly focused on the error by which an image could be represented following reconstruction with spherical symmetric basis functions, with little attention on the effect on spatial resolution.[20,23] In fact, to the best of our knowledge, no previous studies in the literature investigated the impact of the basis function's density function on the spatially variant PSF.

The proposed methodology, which we have previously used to evaluate the PSF on both whole-body PET/CT and brain dedicated PET scanners, was successfully adapted to become MR compatible as the MR magnet was on during the measurements, without any modifications in the phantom design.[14] For all reconstructions we used the standard $2 \times 2 \times 2$ mm^3 voxels which is the minimum that can be achieved during reconstruction by the clinical system. However, using offline reconstruction software we reconstructed data with $1 \times 1 \times 1$ mm^3 voxels which resulted in only a small difference of ~0.1 mm in the FWHM at the optimum basis function parameters and at the center of the FOV. However, the reconstructed PSFs became substantially noisier which resulted in obtaining unreliable parameter estimates during the Gaussian mixture model fitting. Furthermore, the reconstructed times especially for the reconstructions using basis functions with large radius and small alpha parameters became completely impractical, with reconstructions taking up to 2 days to complete. Thus for this study we opted for a $2 \times 2 \times 2$ mm^3 voxel without compromising on the spatial resolution estimates.

In this study, a statistical image reconstruction was used to derive and evaluate the image based PSF. Similar methodology has been used when reporting such measurements.[15,19,26,27] One potential issue with such methods is that the non-negativity constraint could artificially enhance the measurements if a single point source in the air is used. However, in our method we simultaneously scan multiple point sources which should alleviate or minimize any potential problems which could arise if only a single point source was used in the reconstructed FOV, as all the other point sources could be considered as a background to a specific point source. Furthermore, analytical reconstruction, such as FBP, is not available on the system for routine clinical usage.

Using standard basis function parameters, first we evaluated the variation of the image space PSF under spatial transformations. Based on the results presented, the PSF was found to be largely invariant under spatial transformations apart from its radial component, being radially dependent. However, this radially dependent spatial resolution deterioration does not appear to be as significant as compared to other PET systems evaluated with the same methodology.[14] The axial and tangential components on the other hand were found to be invariant throughout the FOV. This is in contrast to reported data from other PET systems where both these PSF

components were found to vary under radial transformations.[14] This difference can be attributed to the list-mode reconstruction used in the Ingenuity PET/MR system, which avoids any axial under-sampling (spanning) of the raw data prior to reconstruction, used by other PET systems. As in a span, the axial displacement between the true and assigned LOR is radially dependent, the axial resolution becomes dependent upon the distance from the scanner's axis, something that is avoided in list-mode based reconstruction and is reflected in the scanner's axial and tangential resolution. Another effect that was seen and could be attributed to the list-mode reconstruction is the axial asymmetry, mainly at extreme axial distance. However, the axial asymmetry was found to be small enough compared to the radial, since the axial FWHM remained invariant under axial transformations.

No direct comparison between having the magnetic field on and off was performed in this study as the scanner operates in a clinical environment and therefore shutting of the magnet was not feasible. However, based on the data collected with the magnet on, no noticeable impact or artifact of the magnetic field on the measured PSFs was observed.[1] In our work, we used fluorine-18 as the isotope of choice; however, in a more energetic isotope, the impact of the magnetic field could be more strongly felt and be enough to influence the overall reconstructed FWHM.

A number of parameters controlling the shape and size of the Kaiser-Bessel basis function were systematically evaluated to assess their impact on the image space PSF and consequently the reconstructed spatial resolution. Based on the presented results, we observed that under certain combination of parameters, spatial resolution starts to degrade. The degradation is uniform in the axial and tangential components, while in the radial component this degradation is seen originally at the center of the radial FOV and progressively extends towards the edge of the FOV depending on the basis function used. Effectively, it is the basis function FWHM that ultimately influences the reconstructed resolution with both the radius and the alpha parameters controlling it. We observed that for a small alpha parameter and as we increase the radius up to 1.9708, no change in the resolution was noticed, while for higher values a clear degradation was observed. The way the basis function parameter induced degradation occurs in the radial FWHM [Fig. 6(a)] indicated that for a basis function FWHM at least equal to the scanner's intrinsic FWHM, no degradation in the reconstructed FWHM could be observed. For a basis function with FWHM higher than that of the scanner's, the reconstructed FWHM starts degrading. This can explain the reason why a combination of parameters degrades the resolution at the center of the FOV and not at the edge. The basis function could have a FWHM higher than that of the scanner at the center of the FOV, in which case the reconstructed resolution will degrade, but since at the edge the intrinsic resolution is worse due to parallax error, the basis function FWHM might still be lower, in which case the reconstructed resolution remains unaffected. The reason of this degradation could possibly be attributed to the fact that the reconstruction using spherical symmetric basis functions can be considered equivalent to a PSF reconstruction in the basis function coefficient space followed by a convolution with the basis density function.[22] Since the FWHM of the basis function is gradually increasing to a point where it becomes larger than that of the system's intrinsic FWHM, no more resolution is recovered in coefficient space no matter how large is the basis function. However, the subsequent convolution with the large basis function will only help to degrade the spatial resolution. Furthermore, the larger the basis function is, the more it changes the shape of the true image space PSF, as the shape becomes dominated by the shape of the basis function shape, something which is demonstrated in Fig. 11. When the basis function's FWHM approaches and becomes larger than the FWHM at the edge of the radial FOV (having the highest intrinsic resolution), the PSF and the spatial resolution become truly spatially invariant, despite the fact that the reconstructed resolution throughout the FOV has degraded overall and reached that at the edge of the radial FOV.

Based on the above, one could use the contour lines in Fig. 12 to select parameters which do not degrade spatial resolution and do not change the PSF. By staying on the left of the 4.2 mm contour line, such a criterion is satisfied but when having to choose the optimum parameters, a better optimization can be made by looking at Fig. 13. This is true since although certain parameters can give optimum spatial resolution, the error and the nonuniformity in the images is so big that the resolution becomes nonuniform with sudden changes in the FOV. This was also confirmed from the phantom and clinical studies, where we deliberately used extreme parameters leading to severe artifacts. Looking as the patient dataset shown in Fig. 16, using optimum error parameters resulted in different spatial resolution estimates between the two sampling distance schemes. Using a value of $d = 2.0375$ resulted in increased blurring compared to $d = 1.0188$, although both parameter combinations comply to the minimum error criterion. We found that using an $r/d = 2.3878$, $a = 10.4101$, and $d = 1.0188$ gave improved cortex delineation and contrast while satisfying the minimum error criterion, However, due to the large radius, such reconstructions can be computationally intensive and other parameter combinations based on Fig. 13 with smaller radius and larger alpha can be used as alternatives. It is though the clinical task which will ultimately impact the choice of the basis function parameters as it is possible to alter the variance properties of the reconstructed images while still maintaining optimum spatial resolution. However, for certain parameter values, spatial resolution degrades as well and it is important to set guidelines for optimum basis function parameter selection which are scanner specific and depending on the system's intrinsic spatial resolution properties. In Fig. 13, it was observed that for $d = 1.0188$, parameters in the first two zero crossings of the Fourier transform of the basis function, minimize both error and resolution. However, although the parameters for a minimum error are fixed and independent of the scanner, the parameters for optimum resolution appear to be scanner-specific and subject to optimization as previously mentioned. As pointed out by Stute and Comtat[22] and also discussed briefly in Sec. 2, using Kaiser-Bessel functions as basis functions, is a user's choice and the image-based PSF derived from a pixel-based

reconstruction could equally be used as a basis function. However, the benefit of having a Bessel function as a basis function for image representation stems from the fact that its individual parameters could be chosen so as to satisfy the aforementioned necessary mathematical conditions, something that is most likely not guaranteed by using the scanner's PSF which has a fixed density function.

6. CONCLUSION

Overall the Ingenuity TF PET/MR, under optimum basis function parameters, exhibits excellent spatial resolution characteristics mainly due to the fact that the raw data are not under-sampled/rebinned enabling the spatial resolution to be dictated by the scanner's intrinsic resolution and the image reconstruction parameters. Due to the impact of these parameters on the resolution properties of the reconstructed images, the image space PSF varies both under spatial transformations and basis function parameter selection. Nonetheless, for a range of basis function parameters, the image space PSF can be considered optimum with the range depending on the scanner's intrinsic resolution properties. Within this range of parameters, the analysis from the point source data could be used to enable the image based PSF to be incorporated within resolution recovery image reconstruction algorithms. However, since it is unique to the range of basis function parameters, it can only be used for the specified range of basis function parameters, used to derive it. Finally, since the Ingenuity PET/MR is comprised of the GEMINI TF PET component and based on the fact of no interference between the PET and MR systems,[1] the findings of this study could potentially be applied on PET/CT systems using the same PET component.[10]

ACKNOWLEDGMENTS

This work was supported by the Swiss National Science Foundation under Grant Nos. SNSF 31003A-135176 and 31003A-149957. The authors would like to thank Susanne Heinzer and Benedicte Delattre (Philips Healthcare) for assisting with data acquisition and handling and Giulia Di Domenicantonio for assisting in the phantom preparation and data acquisition.

[a]Author to whom correspondence should be addressed. Electronic mail: Fotis.Kotasidis@unige.ch

[1]H. Zaidi, N. Ojha, M. Morich, J. Griesmer, Z. Hu, P. Maniawski, O. Ratib, D. Izquierdo-Garcia, Z. A. Fayad, and L. Shao, "Design and performance evaluation of a whole-body ingenuity TF PET-MRI system," Phys. Med. Biol. **56**, 3091–3106 (2011).

[2]P. Veit-Haibach, F. P. Kuhn, F. Wiesinger, G. Delso, and G. von Schulthess, "PET-MR imaging using a tri-modality PET/CT-MR system with a dedicated shuttle in clinical routine," MAGMA **26**, 25–35 (2013).

[3]G. Delso, S. Furst, B. Jakoby, R. Ladebeck, C. Ganter, S. G. Nekolla, M. Schwaiger, and S. I. Ziegler, "Performance measurements of the Siemens mMR integrated whole-body PET/MR scanner," J. Nucl. Med. **52**, 1914–1922 (2011).

[4]S. R. Cherry, A. Y. Louie, and R. E. Jacobs, "The integration of positron emission tomography with magnetic resonance imaging," Proc. IEEE **96**, 416–438 (2008).

[5]H. Zaidi and A. Del Guerra, "An outlook on future design of hybrid PET/MRI systems," Med. Phys. **38**, 5667–5689 (2011).

[6]Y. Shao, S. R. Cherry, K. Farahani, and K. Meadors, "Simultaneous PET and MR imaging," Phys. Med. Biol. **42**, 1965–1970 (1997).

[7]M. S. Judenhofer, H. F. Wehrl, D. F. Newport, C. Catana, S. B. Siegel, M. Becker, A. Thielscher, M. Kneilling, M. P. Lichy, M. Eichner, K. Klingel, G. Reischl, S. Widmaier, M. Rocken, R. E. Nutt, H. J. Machulla, K. Uludag, S. R. Cherry, C. D. Claussen, and B. J. Pichler, "Simultaneous PET-MRI: A new approach for functional and morphological imaging," Nat. Med. **14**, 459–465 (2008).

[8]G. Delso and S. Ziegler, "PET/MRI system design," Eur. J. Nucl. Med. Mol. Imaging **36**, 86–92 (2009).

[9]J. S. Karp, S. Surti, M. E. Daube-Witherspoon, and G. Muehllehner, "Benefit of time-of-flight in PET: Experimental and clinical results," J. Nucl. Med. **49**, 462–470 (2008).

[10]S. Surti, A. Kuhn, M. E. Werner, A. E. Perkins, J. Kolthammer, and J. S. Karp, "Performance of Philips Gemini TF PET/CT scanner with special consideration for its time-of-flight imaging capabilities," J. Nucl. Med. **48**, 471–480 (2007).

[11]S. Yamamoto, H. Watabe, Y. Kanai, M. Aoki, E. Sugiyama, T. Watabe, M. Imaizumi, E. Shimosegawa, and J. Hatazawa, "Interference between PET and MRI sub-systems in a silicon-photomultiplier-based PET/MRI system," Phys. Med. Biol. **56**, 4147–4159 (2011).

[12]A. Rahmim, J. Qi, and V. Sossi, "Resolution modeling in PET imaging: Theory, practice, benefits, and pitfalls," Med. Phys. **40**, 064301 (15pp.) (2013).

[13]V. Y. Panin, F. Kehren, C. Michel, and M. Casey, "Fully 3-D PET reconstruction with system matrix derived from point source measurements," IEEE Trans. Med. Imaging **25**, 907–921 (2006).

[14]F. A. Kotasidis, J. C. Matthews, G. I. Angelis, P. J. Noonan, A. Jackson, P. Price, W. R. Lionheart, and A. J. Reader, "Single scan parameterization of space-variant point spread functions in image space via a printed array: The impact for two PET/CT scanners," Phys. Med. Biol. **56**, 2917–2942 (2011).

[15]E. Rapisarda, V. Bettinardi, K. Thielemans, and M. C. Gilardi, "Image-based point spread function implementation in a fully 3D OSEM reconstruction algorithm for PET," Phys. Med. Biol. **55**, 4131–4151 (2010).

[16]D. B. Wiant, J. A. Gersh, M. C. Bennett, and J. D. Bourland, "PET image reconstruction using LOR-OSEM with a 3D spatially variant system matrix," *IEEE Nuclear Science Symposium Conference Record (NSS/MIC)* (IEEE, Orlando, 2009), pp. 3752–3758.

[17]A. M. Alessio, C. W. Stearns, S. Tong, S. G. Ross, S. Kohlmyer, A. Ganin, and P. E. Kinahan, "Application and evaluation of a measured spatially variant system model for PET image reconstruction," IEEE Trans. Med. Imaging **29**, 938–949 (2010).

[18]C. C. Watson, L. Eriksson, and A. Kolb, "Physics and applications of positron beams in an integrated PET/MR," Phys. Med. Biol. **58**, L1–L12 (2013).

[19]A. J. Reader, P. J. Julyan, H. Williams, D. L. Hastings, and J. Zweit, "EM algorithm system modeling by image-space techniques for PET reconstruction," IEEE Trans. Nucl. Sci. **50**, 1392–1397 (2003).

[20]R. M. Lewitt, "Alternatives to voxels for image representation in iterative reconstruction algorithms," Phys. Med. Biol. **37**, 705–716 (1992).

[21]R. M. Lewitt, "Multidimensional digital image representations using generalized Kaiser-Bessel window functions," J. Opt. Soc. Am. A **7**, 1834–1846 (1990).

[22]S. Stute and C. Comtat, "Practical considerations for image-based PSF and blobs reconstruction in PET," Phys. Med. Biol. **58**, 3849–3870 (2013).

[23]S. Matej and R. M. Lewitt, "Practical considerations for 3-D image reconstruction using spherically symmetric volume elements," IEEE Trans. Med. Imaging **15**, 68–78 (1996).

[24]S. Matej and R. M. Lewitt, "Efficient 3D grids for image reconstruction using spherically-symmetric volume elements," IEEE Trans. Nucl. Sci. **42**, 1361–1370 (1995).

[25]W. Wang, Z. Hu, E. E. Gualtieri, M. J. Parma, E. S. Walsh, D. Sebok, Y.-L. Hsieh, C.-H. Tung, X. Song, J. J. Griesmer, J. A. Kolthammer, L. M. Popescu, M. Werner, J. S. Karp, and D. Gagnon, "Systematic and distributed time-of-flight list mode PET reconstruction," IEEE Nucl. Sci. Symp. Conf. Rec. **3**, 1715–1722 (2006).

[26]F. C. Sureau, A. J. Reader, C. Comtat, C. Leroy, M.-J. Ribeiro, I. Buvat, and R. Trebossen, "Impact of image-space resolution modeling for studies with the High-Resolution Research Tomograph," J. Nucl. Med. **49**, 1000–1008 (2008).

[27]C. Cloquet, F. C. Sureau, M. Defrise, G. Van Simaeys, N. Trotta, and S. Goldman, "Non-Gaussian space-variant resolution modelling for list-mode reconstruction," Phys. Med. Biol. **55**, 5045–5066 (2010).